GasHis-Transformer: A Multi-scale Visual Transformer Approach for Gastric Histopathology Image Classification

Haoyuan Chen^{*a*,1}, Chen Li^{*a*,*,2}, Xiaoyan Li^{*b*,*,3}, Ge Wang^{*c*,5}, Weiming Hu^{*a*,5}, Yixin Li^{*a*,6}, Wanli Liu^{*a*,7}, Changhao Sun^{*a*,*d*,*e*,8}, Yudong Yao^{*f*,9} and Marcin Grzegorzek^{*d*,10}

ARTICLE INFO

Keywords: Grastic histropathology image Multi-scale visual transformer Image classification

ABSTRACT

For deep learning methods applied to the diagnosis of gastric cancer intelligently, existing methods concentrate more on Convolutional Neural Networks (CNN) but no approaches are available using Visual Transformer (VT). VT's efficient and stable deep learning models with the most recent application in the field of computer vision, which is capable of improving the recognition of global information in images. In this paper, a multi-scale visual transformer model (GasHis-Transformer) is proposed for a gastric histopathology image classification (GHIC) task, which enables the automatic classification of gastric histological images of abnormal and normal cancer by obtained by optical microscopy to facilitate the medical work of histopathologists. This GasHis-Transformer model is built on two fundamental modules, including a global information module (GIM) and a local information module (LIM). In the experiment, an open source hematoxylin and eosin (H&E) stained gastric histopathology dataset with 280 abnormal or normal images are divided into training, validation, and test sets at a ratio of 1:1:2 first. Then, GasHis-Transformer obtains precision, recall, F1-score, and accuracy on the testing set of 98.0%, 100.0%, 96.0%, and 98.0%. Furthermore, a contrast experiment also tests the generalization ability of the proposed GatHis-Transformer model with a lymphoma image dataset including 374 images and a breast cancer dataset including 1390 images in two extended experiments and achieves an accuracy of 83.9% and 89.4%, respectively. Finally, GasHis-Transformer model demonstrates high classification performance and shows its effectiveness and enormous potential in GHIC tasks.

1. Introduction

Cancer is a malignant tumor that originates from epithelial tissue and is the most common type of malignant tumor [1]. As one of the deadliest diseases, cancer caused approximately 9.6 million deaths in 2018, the highest number since records began in the 1970s. Of all cancer categories, gastric cancer has the second highest cancer rate in the world in terms of morbidity and mortality [2]. Gastric cancer is a collection of abnormal cells that form tumors in the stomach. In histopathology, the most common type of gastric malignant tumor is adenocarcinoma, which starts in mucous-producing cells in the inner layer of the stomach that tend to invade the stomach wall, infiltrating the muscular mucosa, and then invade the outer muscular. About 800,000 people die of the disease every year, according to World Health Organization statistics [3]. In countries around the world, the number of gastric cancer patients is rising faster than the number of non-cancer patients. It is estimated that about 30,000 new cases of gastric cancer occur each year [4]. Therefore, it is very important for medical staff to accurately diagnose gastric cancer.

The diagnosis of gastric cancer depends on a careful ex-

*Corresponding author

lichen201096@hotmail.com (C. Li); lixiaoyan@cancerhosp-ln-cmu.com (X. Li) amination of Hematoxylin and Eosin (H&E) stained sections by pathologists under a microscope. It is time-consuming and subjective to observe tissue slices under a microscope [5]. Because of these shortcomings, pathologists have a great deal of difficulty with accurate screening and diagnosis of gastric cancer. Thus, computer-aided diagnosis (CAD) that began in the 1980s can reduce these shortcomings by making diagnostic decisions and improving efficiency [6]. The goal of CAD is to improve the quality and efficiency of radiologists by improving the accuracy and consistency of radiological diagnosis and increasing the number of images taken in a short amount of time [7]. Over the past few decades, researchers have conducted extensive research on the design of CAD that helps doctors diagnose cancer and treat the disease.

With the advent of the era of artificial intelligence, deep learning becomes the most extensive and most widely used method of computer-aided diagnosis [8]. Deep learning results in many achievements in search technology, data mining, machine learning, machine translation, natural language processing, multimedia learning, computer vision, recommendation algorithms, and personalization technology, as well as other related fields. Deep learning enables a computer to imitate human activities such as audio-visual and thought, solves many complex pattern recognition problems,

^aMicroscopic Image and Medical Image Analysis Group, MBIE College, Northeastern University, 110169, Shenyang, PR China

^bDepartment of Pathology, Cancer Hospital, China Medical University, Liaoning Cancer Hospital and Institute,110042, Shenyang, PR China

^cDepartment of Biomedical Engineering, Rensselaer Polytechnic Institute, 12180, Troy, New York, USA

^dInstitute of Medical Informatics, University of Lübeck, 23538, Lübeck, Germany

^eUniversity of Chinese Academy of Sciences, 100049, Beijing, PR China

^fDepartment of Electrical and Computer Engineering, Stevens Institute of Technology, 07030, Hoboken, New Jersey, USA

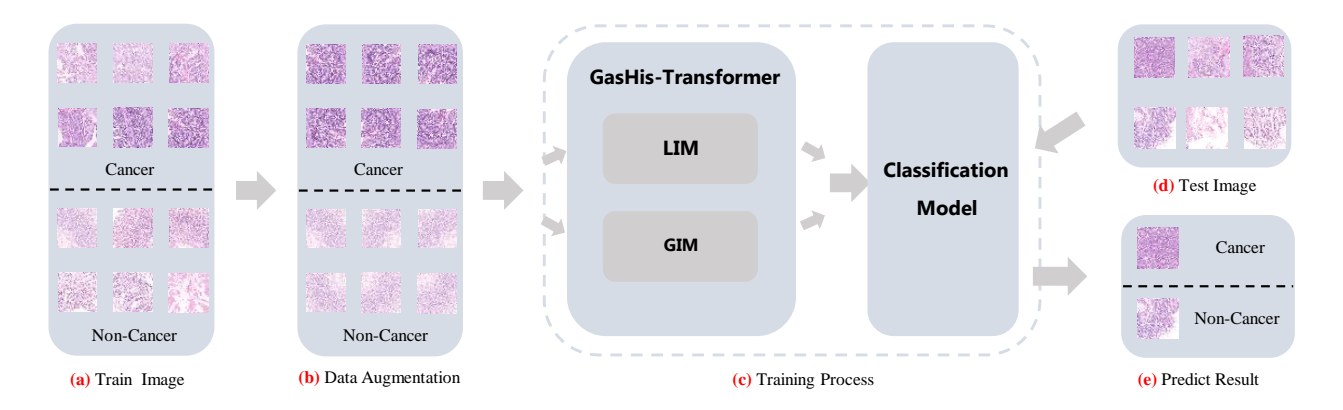


Figure 1: The GasHis-Transformer model architecture.

and is making great progress in artificial intelligence-related technology now [9]. In the field of computer vision, *Convolutional Neural Networks* (CNN) models are the dominant type of deep learning that can be applied to many tasks [10]. However, CNN models have some shortcomings, one of which is that CNN models do not handle global information well. In contrast, the novel *Visual Transformer* (VT) models applied in the field of computer vision can support more abundant global information. Based on CNN and VT models mentioned above, a hybrid model is heuristically proposed for *Gastric Histopathology Image Classification* (GHIC) tasks, namely GasHis-Transformer, to integrate the local and global information into an organic whole. The training flow chart is shown in Fig. 1.

The proposed model can be understood as an early fusion of a transformer model and a CNN model. The whole model is made up of two modules, namely Global Information Module (GIM) and Local Information Module (LIM). Based on ResNet-50 model proposed in 2015 [11], the modified BoTNet-50 model is the latest VT model used in computer vision to achieve high-performance image processing capabilities. In the proposed model, all structures of BoTNet-50 model before full connection layer (FC Layer) are preserved in GIM are preserved. In LIM, the structure of some Inception-V3 models is applied to the proposed model. The Inception-V3 model is a classical CNN model of parallel structure[12]. Finally, the previous two blocks using the FC Layer and the softmax layer are used to export the features to output the classification results.

This study presents an exhaustive analysis of fusion CNN and VT models to develop a better classification model for GHIC tasks. The novel contributions of this study are as follows. First, considering the advantages of CNN models in dealing with local features and VT models in dealing with global features, a new model framework is proposed. the proposed model integrates the two models with the 2048-dimensionalities features extracted from the two models into 4096-dimensionalities features, which are the output of the extracted features. Second, because of the multi-scale characteristics of a histopathological image under a microscope.

In combination with the current situation, the proposed model chooses the Inception-V3 model to deal with multi-scale problems well in many CNN models.

This article is organized with five sections: Section 2 provides a review of the current status of GHIC tasks in the past few years, Section 3 provides the details of the proposed methodology, Section 4 presents experimental result, discussion, comparison with previous studies found in recent literature, and expansion experiment. Finally, Section 5 concludes the work and provides future research guidelines.

2. Related Work

2.1. Image Classification in gastric histopathology research

In GHIC tasks, machine learning is a traditional method that has been used for many years [13]. In [3], 31 features based on color, texture, and morphology extracted from each patch image are classified by an AdaBoost classifier and the final image classification result is obtained by combining the classification results of each patch. In [14], Random Forest (RF) classifier is used to classify 332 global graph features including the mean, variance, skewness, kurtosis, and other features extracted from gastric cancer histopathology. In [15], after feature dimensionality reduction, Local Binary Patterns (LBP) and Histograms of Oriented Gradient (HOG) features are classified and compared by RF and Artificial Neural Network (ANN) classifiers. The ANN classifier is superior to the RF classifier. In [16], Three comparative experiments are carried out. K-Singular Value Decomposition (K-SVD) is used to learn the features extracted from the CNN, and then sparse decomposition is carried out. Finally, a 95% classification accuracy is obtained.

In recent years, deep learning methods have become increasingly used in GHIC tasks. In [17], the improved ResNet-v2 network is used to classify images by adding an average pooling layer and a convolution layer. Finally, the classification accuracy of the model is 86.5%. In [18], 2166 whole slide images (WSIs) are classified by a deep learning model based on DeepLab-V3 with ResNet-50 architec-

ture as the backbone and the accuracy, sensitivity, and specificity of the model are 87.3%, 99.6% and 84.3%, respectively. In [19], a multi-scale receptive field depth neural network based on Inception-V3 model is proposed to analyze the histopathological images in WSIs. In [20], a network is proposed to combine AlexNet, ResNet-50, and Inception-V3, and then uses ten-fold validation to test the classification performance. Finally, all the ten-fold validation results are used to calculate the accuracy, sensitivity, and specificity.

2.2. Overview of deep learning methods

The first application of deep learning network is LeNet proposed by LeCun et al. in 1989 [10]. However, due to poor computing power, limited relative technology, and negligible available data for analysis, deep learning does not exhibit excellent recognition performance in image classification. In 2012, Hinton et al. proposed AlexNet and used Compute Unified Device Architecture (CUDA) to accelerate the training of deep learning models for the first time. AlexNet uses the powerful parallel computing ability of the graphics processing unit to process a large number of matrix operations in the training of deep learning model [21]. Since then, deep learning methods have formally replaced traditional machine learning methods. VGG model was proposed by the Visual Geometry Group at the University of Oxford in 2014. Its novelty contribution is raising the depths of networks from eight to sixteen or nineteen which is named VGG-16 and VGG-19, and turning large convolution kernels such as $7 \times$ 7 and 5×5 into three or two 3×3 small convolution kernels [22]. It is one of the milestones in deep learning after AlexNet and also the baseline for comparing new methods in deep learning field. VGG model has substantial advantages. First, VGG model uses the small convolution kernel to reduce parameters and improve the recognition accuracy. Second, VGG structure is consistent and suitable for parallel acceleration. Finally, the particularly important contribution is providing a clear direction for deep learning networks: increasing network depth [23]. However, VGG model also has some celebrated disadvantages. VGG model only increases the number of network layers to make too many parameters, resulting in a long training time. In addition, when VGG model reaches a certain depth, the gradient simply disappears, which makes the model difficult to optimize.

Inception-V3 model is the other method to modify AlexNet and based on the GoogLeNet proposed by Szegedy et al. in 2015 [24]. Instead of using the conventional method to increase the number of network layers, Inception-V3 uses a novel convolution method to decompose the large filter sizes: using parallel convolution and factorized convolution in the same receptive fields, and the whole decomposition module is called the inception structure. Inception-V3 network has five different inception structures, each with its own set of components. The five different inception structures are shown in Fig. 2. Inception-V3 model has obvious merits. Inception-V3 model uses inception module instead of large convolution kernel and global average pooling layer instead

of FC layer to prominently reduce the number of parameters compared with other networks which increased network layers so that it has an excellent performance on large-scale data sets and mobile devices with poor computing ability [23]. However, the fatal drawback of Inception-V3 model is that training is very difficult and even cannot lead to convergence when the network depth is increasing.

ResNet model proposed by He et al. in 2015 perfectly

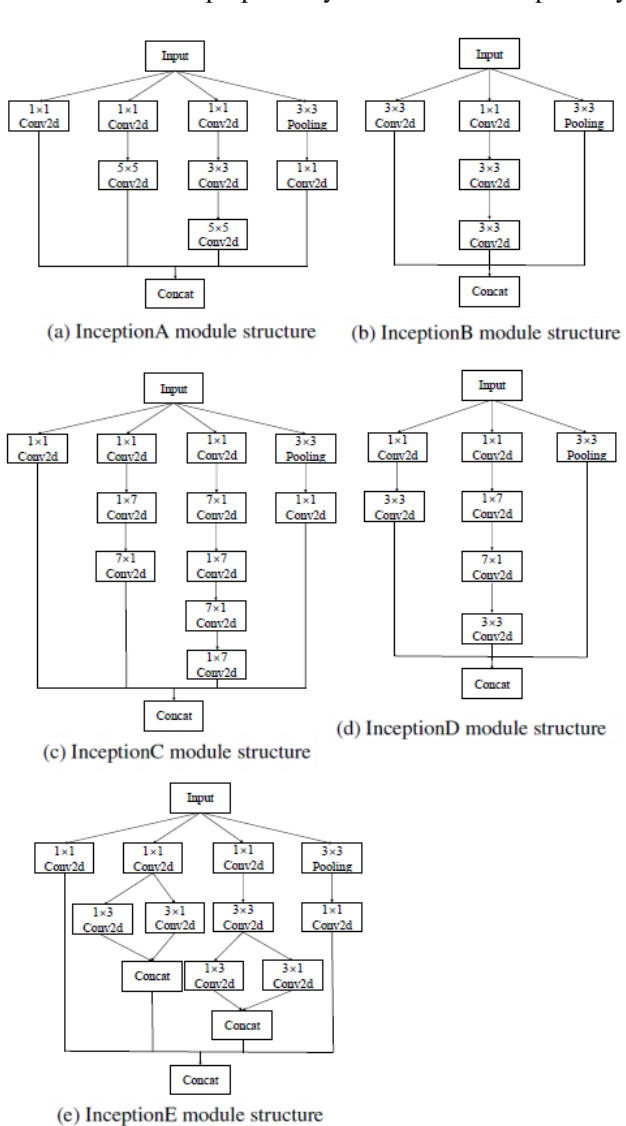


Figure 2: Five different structures of Inception-V3 model.

solves the shortcomings of VGG and Inception-V3 by increasing the number of network layers leading to the disappearance of gradients and the non-convergence of the model. ResNet model is named ResNet-18, ResNet-32, ResNet-50, ResNet-101, ResNet-152 according to the number of 18, 32, 50, 101, 152 network layers [11]. The main contribution of ResNet model is to propose residual structure and apply residual structure to deep learning networks for the first time. There are two main design ideas for residuals: shortcut connection and identity mapping. Shortcut connection makes residuals possible and identity mapping makes the network

deeper. The residual learning unit of ResNet model is to connect results of multiple convolution layers with an Identity mapping using a shortcut connection by ReLU activation function. There are two types of residual unit structures, namely, two-layer residual unit and three-layer residual unit. Two-layer residual units are used in shallower network layers such as ResNet-18 and ResNet-32, and threelayer residual units are used in models with deeper network layers such as ResNet-50 and ResNet-101 and so on [11]. ResNet model, as the first network to present the widely used residual structure, has many remarkable advantages. First of all, it is of epoch-making significance that ResNet model introduces residual structure to solve the model degeneration problem caused by the deepening network layer. Secondly, Resnet model uses normalized initialization and intermediate normalized layer to better solve the problem of gradient disappearance. However, ResNet model has some common shortcomings of CNN models, such as the parameters used to increase the pooling layer of the receptive field cannot be trained and the model has poor ability to extract features from small objects [25].

Inspired by deep separable convolution [26], Xception is an improvement of Inception-V3 proposed by Google [12, 27]. Xception divides depthwise separable convolution into depthwise convolution and pointwise convolution to improve Inception structure. Concomitantly, residual connection [11] is used in each block instead of concat in the original Inception structure. The advantage of Xception is that it combines the residual structure and inception structure to integrate their advantages, and depthwise separable convolution reduces the complexity of the network, which makes the network model easy to convergence [28]. However, Xception also inherits the shortcomings of CNN models, in that the model has poor ability to extract global features.

In recent years, VT [29] models, which are widely used in natural language processing, are more and more used in computer vision classification, segmentation, target detection, and other fields [30]. VT models are realized by attention mechanism [29]. There are two main forms of transformer model in computer vision classification task, that is the pure self-attention structure represented by ViT and the self-attention structure combined CNN models represented by BotNet-50 [31, 32, 33]. The biggest advantage of transformer models is that it perfectly solves the shortcomings of CNN models. VT models can better describe the global information of images and have a good ability to extract global information by introducing an attention mechanism. Similarly, VT models also have some disadvantages. The excellent performance of the transformer model in natural language processing depends on the data scale of at least one million. However, most datasets applied in the field of computer vision are in thousands. Therefore, the effect of ViT in dealing with small or medium-sized datasets, such as Imagenet, is not even as good as ResNet model, and it performs well only on large-scale datasets [33].

3. Method

3.1. Vision Transformer (ViT)

The first model for training large-scale datasets using Transformer instead of standard convolution in CV field is Vision Transformer ViT) [32, 33]. An overview of ViT model is shown in Fig. 3. To handle 2D pictures, similarly, as 1D sequences, a 2D patches sequences $x_p \in \mathbb{R}^{N \times (P^2 \times C)}$ are obtained by reshaping the original picture $x \in \mathbb{R}^{H \times W \times C}$. C is the number of picture's channels, $(H \times W)$ is the size of each original picture, (P^2) is the size of each picture patch, $N = HW/P^2$ is the sum of the number of patch as the same as input sequences length of the transformer encoder. Because the invariant hidden vector size D which is used in the transformer go through all of layers of transformer, all patches are flatten to D dimensions, and D dimensions are mapped by a linear projection which can be trained named patch embeddings. To retain positional information, the sequence of embedding vectors that combine standard 1D position embedding and patches embedding is selected to be the input of the transformer encoder.

Transformer encoder is composed of multiple alternate

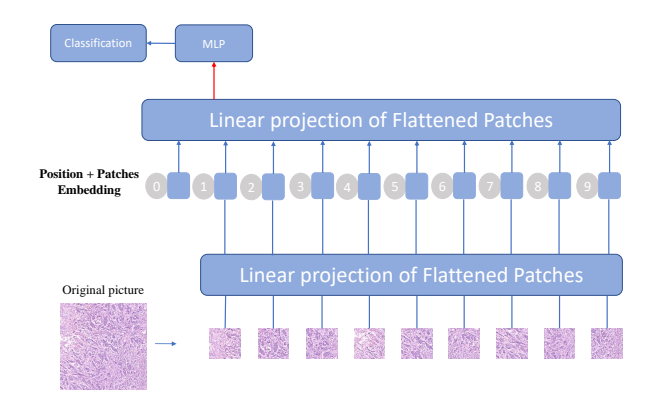


Figure 3: An overview of vision transformer model training process.

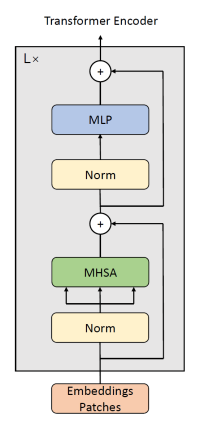


Figure 4: An structure of transformer encoder.

Multi Head Self-Attention (MHSA) blocks [31] and MLP blocks [29]. A structure of transformer encoder is shown

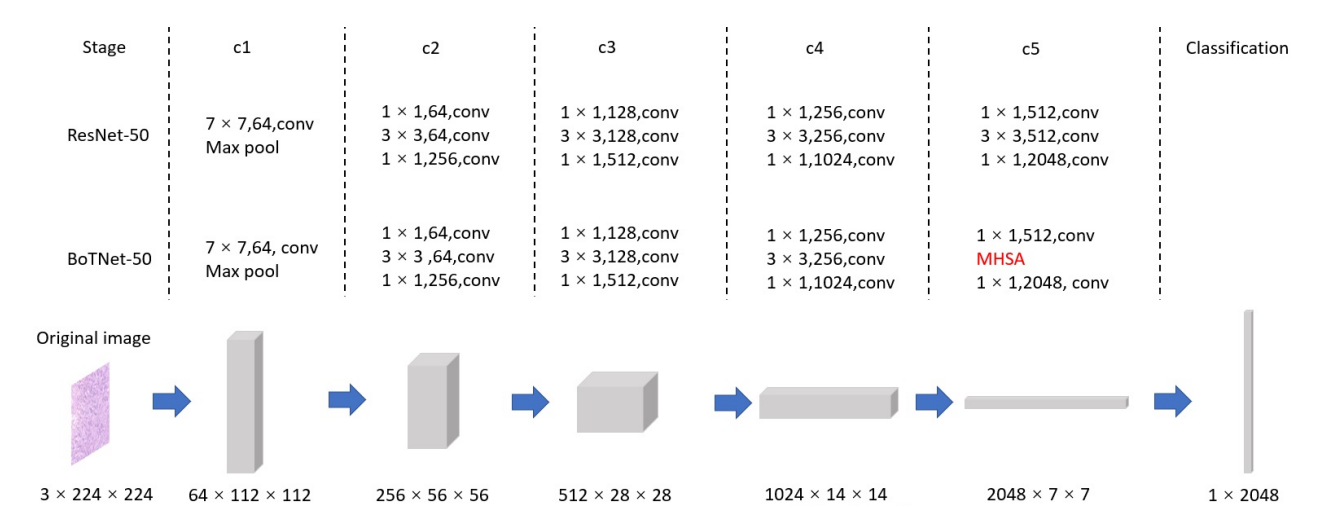


Figure 5: An architecture of BoTNet-50 model and compared with ResNet-50.

in Fig. 4. Layernorm (LN) is used in front of each layer and connected to the following block through residual connection. MLP block has two layers of network, which is connected by a non-linear GELU activation function.

Finally, in classification, an MLP block with a hidden layer is used to train the features which are trained by transformer encoder. And at the fine-tuning time, only a single linear layer is used.

3.2. BoTNet

BoTNet-50 [31] is a novel VT model which combines ResNet-50 of CNN model with the MHSA layer. Because the usage of the MHSA layers reduces massive parameters, BoTNet-50 is a network with a simple structure and powerful functions. An architecture of BoTNet-50 model and compared with ResNet-50 is shown in Fig. 5. BoTNet-50 is not used sophisticated and luxuriant structure, only makes some basic modifications on ResNet-50. Similarly to the hybrid model of ViT [33], in which input sequence extracted from CNN models to alter raw image patches, BoTNet-50 remains the model of ResNet in advance of stage c4 and using the MHSA layers substitute for the last three 3×3 spatial convolutions in stage c5 of the model of ResNet. Thus, BoTNet-50 obtains the global self concern in 2D feature map. The latter part is the same as ResNet-50. The average pooling layer and FC layer are used to extract features and obtain classification results.

There are also different places between BoTNet-50 and ViT. The main difference is that the MHSA [29] of ViT uses standard 2D sequences position encoding, while BoTNet-50 uses 2D relative position encoding. The latest results [34, 35, 36] show that relative position encoding is more suitable for visual tasks than traditional encoding. A structure of relative position encoding of the MHSA is shown in Fig. 6. There is four single-headed attention in each MHSA layer of BoTNet-50. At present, this figure only takes one single-headed attention for example. First, for giving a pixel $x_{ij} \in \mathbb{R}$, we extract $ab \in N_k(i,j)$ from the spatial extent k which centered on x_{ij} . Second, W_O , W_K , W_V as the learnable transforms,

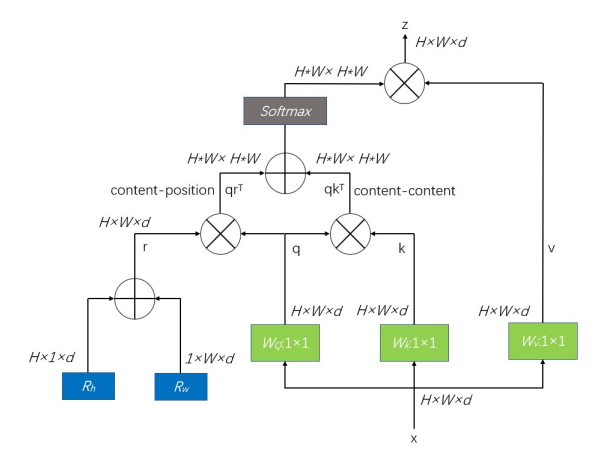


Figure 6: An structure of relative position encoding of the MHSA. \oplus and \otimes express sum and matrix multiply respectively.

-1, -1	-1, 0	-1, 1	-1, 2
0, -1	0, 0	0, 1	0, 2
1, -1	1, 0	1, 1	1, 2

Figure 7: An single example of relative distance computation. The relative distance in the figure is calculated according to the bright position. red is row offset, blue is column offset.

can compute the queries $q_{ij} = W_Q x_{ij}$, keys $k_{ab} = W_K x_{ab}$ and values $v_{ab} = W_V x_{ab}$ which are linear transformations of the pixels of spatial extent. The content information has multiplied the queries and keys value vectors. Third, R_h and R_w as the separable relative position encodings of height and weight are expressed by row offset a-i and column offset b-j. The row offset and column offset is shown in Fig. 7. The row offsets and column offsets are connected with an embedding r_{a-i} and r_{b-j} . The row offset and column offset

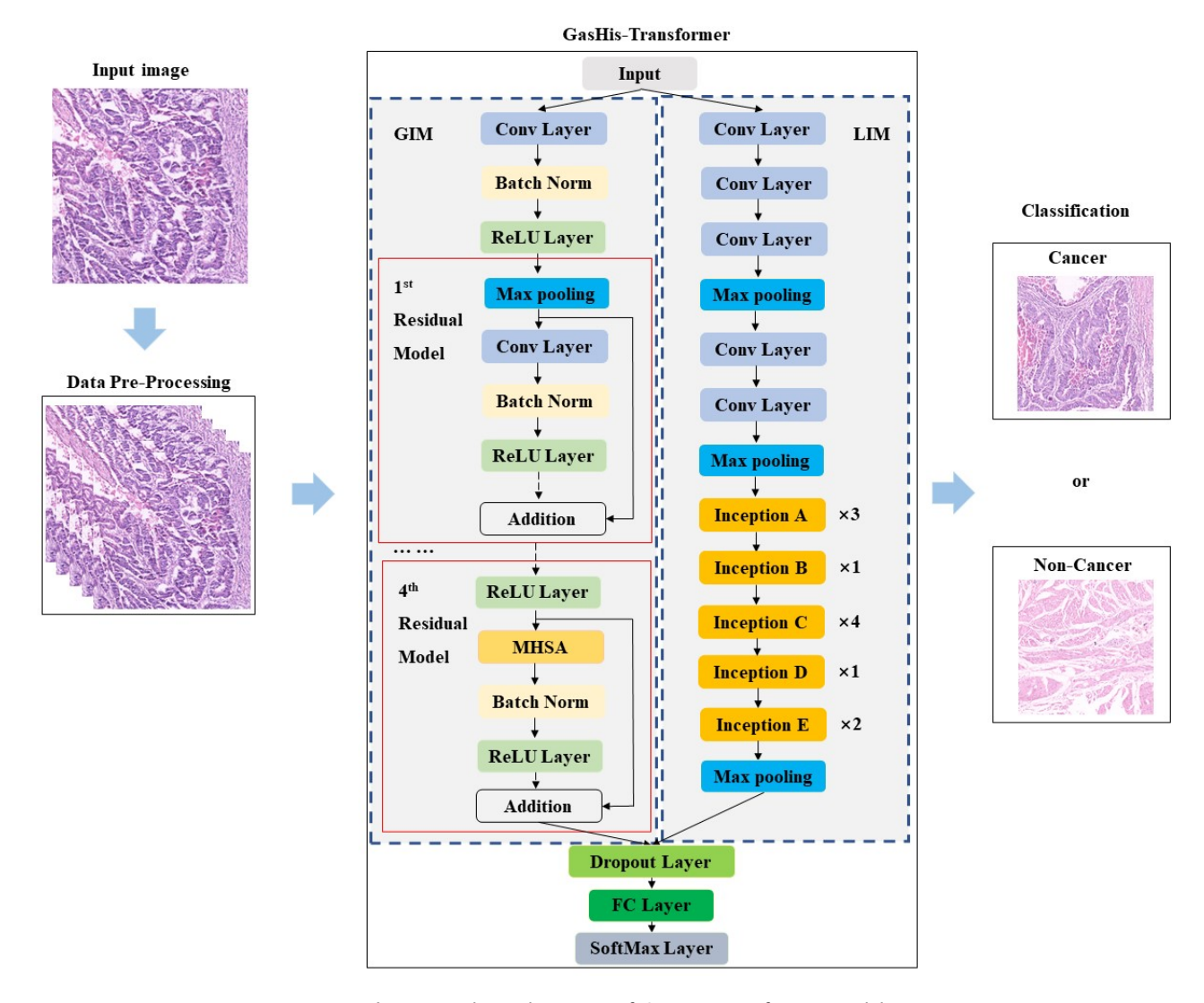


Figure 8: The architecture of GasHis-Transformer model.

embeddings called the position information are connected to form $r_{a-i,b-j}$. Finally, the position information and content information are accumulated, and then the spatial-relative attention y_{ij} (1) of the pixel x_{ij} is obtained by multiplying the aggregation results with values through softmax [35].

$$y_{ij} = \sum_{a,b \in N_k(i,j)} softmax_{ab} (q_{ij}^\intercal k_{ab} + q_{ij}^\intercal r_{a-i,b-j}) v_{ab} \ (1)$$

The number of parameters in MHSA layer is different from that in convolution layer. The number of parameters in convolution increases at a quadratic rate with the increase of spatial extent, while the MHSA layer does not change with the change of spatial extent. When the size of input and output is the same, the computational cost of MHSA layer is far less than that of convolution in the same spatial extent. For example, when the input and output are 128-dimensionalities, the computational cost of 3 spatial extents in the convolution layer is the same as that of 19 spatial extents in the MHSA layer [35]. Therefore, the parameters and computation time of BoTNet-50 are smaller than ResNet-

50 [31].

3.3. GasHis-Transformer

GasHis-Transformer model is proposed which can classify gastric cancer histopathological images. and its architecture is shown in Fig. 8.

At the beginning of the whole process, the input image is pre-processed to improve the quality of the image. Because the color of gastric cancer histopathological image is too shallow and the boundary characteristics of the nucleus are not evidence, resulting in the image quality is poor, GasHis-Transformer uses image normalization to improve the image quality [37]. Image normalization remains the whole image information, only modifies the pixels to a specified range to accelerate the convergence of training network. The specific role of normalization is to summarize the statistical distribution of unified samples. The deep neural network is trained or predicted by the statistical probability of samples in events. When the input image pixels of all samples are positive, the weights connected with the first hidden layer

neurons can only increase or decrease at the same time, resulting in a slow learning speed. To avoid this situation and speed up the network learning speed, the input image pixels can be normalized, so that the mean and variance of the input pixels of all samples are very small [37]. Furthermore, because of the multi-scale characteristics of histopathological images under the microscope, The model expands the image by rotating, mirror, and other data expansion operations. Thus, GasHis-Transformer improves accuracy from two aspects before data into traditional deep learning methods for classification.

After pre-processing, images are used as the input of the proposed model to train the network parameters, and this step is the core of the whole process. GasHis-Transformer includes two parts: Global Information Module (GIM) and Local Information Module (LIM). In GIM, GasHis-Transformer slightly modifies BoTNet-50 network which convolution layer in the last residual layer of the ResNet-50 model is replaced by the MHSA [31]. GIM retains all the structures before c5 stage of BoTNet-50 in GIM, and 2048-dimensionalities global features are extracted in the last pooling layer of GIM. In LIM, GasHis-Transformer bases partly on Inception-V3 model and makes some modifications to the traditional network. To match the standard input of GIM and make the features extracted by GIM and LIM in the whole network the same in measurement, LIM modifies the standard input size of Inception-V3 [12] model from 299×299 to 224×224 and modifies the standard output size of every convolution layer and pooling layer in our proposed model. Similar to GIM. 2048-dimensionalities local features are also extracted in the last pooling layer of LIM. At the end of GIM and LIM, the global feature and local feature are fused to obtain the 4096dimensionalities splicing feature as the final feature trained. Because too many extracted features can increase the probability of extracting noise leading to overfitting [38], GasHis-Transformer adds a dropout layer after concatenating features and filter out irrelevant features such as noise by discarding neurons with a certain probability [39, 40]. Since the number of features extracted from each network in series with GIM and LIM is doubled, GasHis-Transformer set the probability to 0.5 and randomly discard half of them. Finally, GasHis-Transformer takes the output from the dropout layer as the input FC layer, and output it through the softmax [41] function. The highest probability result is the classification of the results of gastric cancer.

The whole proceeding of the proposed GasHis-Transformer network is shown in Algorithm 1.

4. Experiment and analysis

4.1. Experimental Setting

4.1.1. Dataset

In this paper, The dataset for the experiment uses an open source Haematoxylin and Eosin (H&E) stained gastric histopathological image dataset to analyze the performance of GasHis-Transformer model [42]. Some examples of normal and abnormal gastric histopathological images are shown in Fig. 9.

Algorithm 1 GasHis-Transformer Framework

Input: The images used for training, X_{train} ; The images used for validation, X_{val} ; The images used for testing, X_{test} ; The training epoch N:

Output: The classification presentation of the testing images y_{test} of X_{test}

- 1: Image normalization $\widetilde{X}_{\text{train}} = \frac{X_{\text{train}} \overline{X}_{\text{train}}}{\sigma}$; 2: **for** current training steps n in N **do**
- Divide $\widetilde{X}_{\text{train}}$ into patches and put them into model; 3:
- Extract global information $z_g = GIM(\widetilde{X}_{train});$ 4:
- Extract local information $z_l = LIM(\widetilde{X}_{train});$ 5:
- connect global and local information as extracted 6: feature of model $z = [z_g, z_l]$;
- Random abandonment of neurons $\tilde{z} = \text{Dropout}(z)$; 7:
- Classification result through the full connection layer and softmax layer classification $y_{\text{train}} =$ Softmax($FC(\tilde{z})$);
- Model parameters $\{W_1, ..., W_n\}$ are obtained by back propagation of the error by the optimizer;
- Put X_{val} into parameters of model $\{W_1, ..., W_n\}$ and 10: get classification result accuracy acc;
- if The classification accuracy acc is the highest then 11: 12: Store the parameters of model $\{W_1, ..., W_n\}$;
- 13: **for** image x in X_{test} **do**
- Put x into parameters of model $\{W_1, ..., W_n\}$ and get classification result y_{test} ; **return** y_{test} of X_{test}

Gastric histopathological images pass through H&E stained. Hematoxylin staining solution is alkaline, which makes chromatin in the nucleus and ribosome in cytoplasm purple-blue. Eosin staining solution is acidic, which makes the components in cytoplasm and extracellular matrix red [43]. The images are part of the whole slide images (WSIs). The images are augmented 20 times and the image size is 2048 × 2048 pixels [44]. The image format is '*.tiff'. The gastric histopathological image dataset includes 140 normal images and 560 abnormal images. In the normal images, the nuclei are stable and arrange regularly, and the nucleo-cytoplasmic ratio is small. On contrary, in the abnormal images, the nucleus is abnormally large and irregular in features of dish or crater.

4.1.2. Data settings

The dataset set is shown in Table 1. Due to the imbalance of the initial training dataset, the deep learning model only learns the characteristics of one category, which leads to low classification accuracy and weak generalization ability of the model. In GHIC tasks, GasHis-Transformer equally uses the 140 abnormal images and 140 normal images. The abnormal and normal images in the dataset are partitioned into training, validation, and test sets randomly at a ratio of 1:1:2.

In GHIC tasks, information of data augmentation for the image is represented in Table 2. All images are flipped horizontally and vertically and rotated 90, 180, 270 degrees to

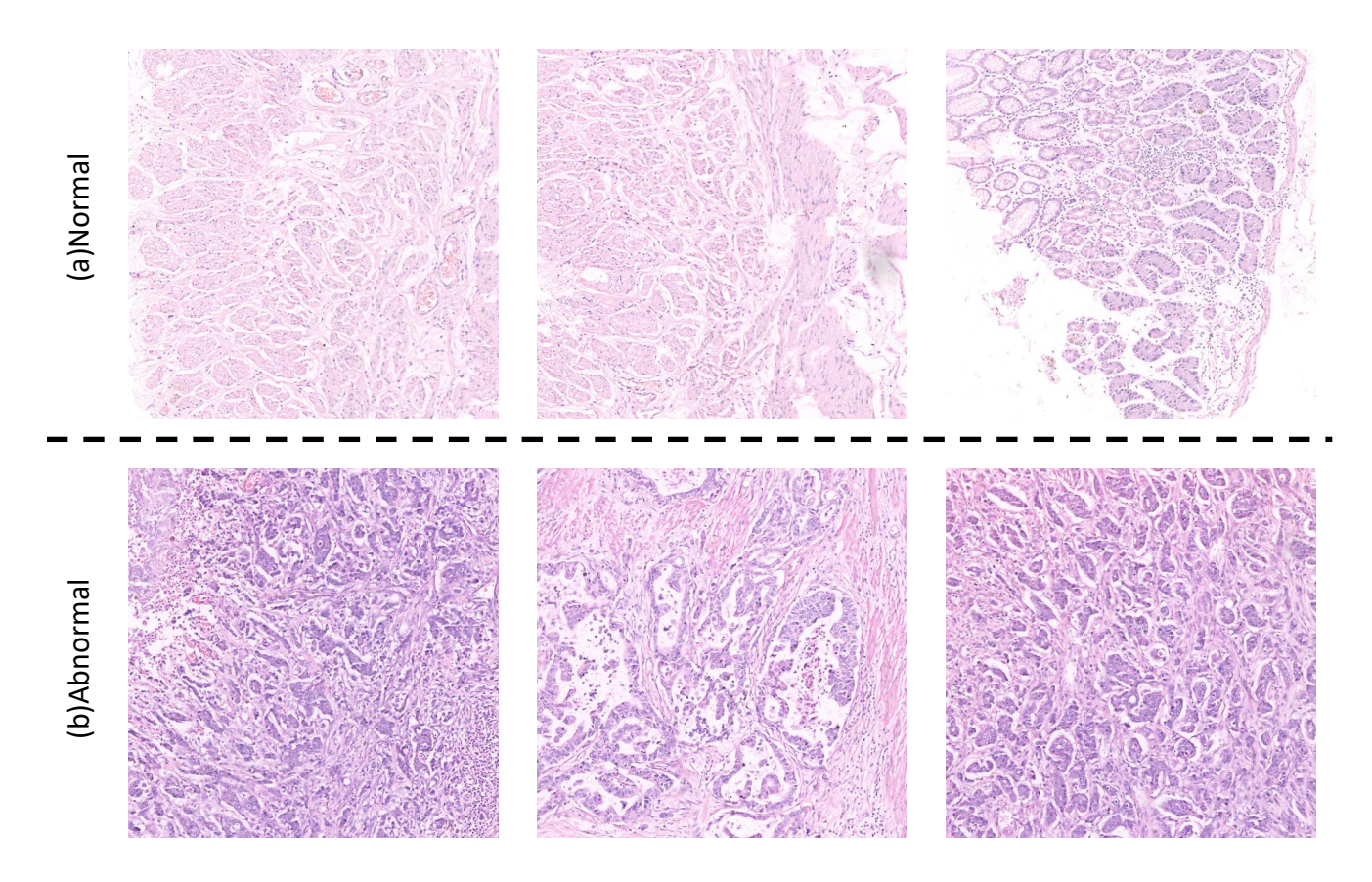


Figure 9: Some examples in the gastric histopathological image dataset.

 Table 1

 Distribution of gastric histopathological data for training, validation and testing.

Image tpye	Training	Validation	Test	Sum
Normal	35	35	70	140
Abnormal	35	35	70	140

 Table 2

 Data augmentation for training, validation and testing.

Image tpye	Training	Validation	Test	Sum
Normal	210	210	420	840
Abnormal	210	210	420	840

augment the training, validation, and testing datasets six times. Furthermore, because the measurement of the gastric histopathological image datasets is too considerable to process, all images are resized to 224×224 pixels by bilinear interpolation [45].

4.2. Classification evaluation

4.2.1. Experimental result

To evaluate the GasHis-Transformer model, The experimental result is statistical classification performance, including accuracy, precision, recall, F1-score, and confuse matrix

 $\begin{tabular}{ll} \textbf{Table 3}\\ \textbf{The four evaluation criteria and corresponding definitions.} \end{tabular}$

Criterion	Definition	Criterion	Definition
Accuracy	TP+TN TP+TN+FP+FP	Precision	TP TP+FP 2×TP
Recall	TP TP+EN	F1-score	2×TP 2×TP±EP±EN

as criteria of GHIC tasks. These four criteria are defined in Table 3. In the definition of these four criteria, TP is the abbreviation of true positive, that is, positive samples are precisely judged as positive samples. TN is the abbreviation of true negative, that is, negative samples are precisely judged as negative samples. FP is an abbreviation of false positive, that is, negative samples are unjustifiably determined as positive samples. FN is an abbreviation of false negative, that is, positive samples are unjustifiably determined as negative samples. Accuracy is the most typical and fundamental evaluation metric. Precision is the ratio of the amount of relevant information retrieved to the total amount of information retrieved, which indicates how many of the predicted positive samples are real positive samples. Recall is the ratio of the total amount of relevant information in the retrieved information system, which indicates how many positive samples in the sample have been correctly predicted. F1-score is a comprehensive consideration of precision and recall, and it

0	206 0.4905	1 0.0023	0.9952 0.0048	0	403 0.4905	0 0.0000	1.0000 0.0000
Output Class	4 0.0095	209 0.4976	0.9812 0.0187	Output Class	17 0.0095	420 0.5000	0.9610 0.0389
	0.9810 0.0190	0.9952 0.0048	0.9881 0.0119		0.9595 0.0405	1.0000 0.0000	0.9797 0.0202
•	0	`> Target Class		•	0	> Target Class	
	(a) Confusion matrix on the validation set				(b) Confusio	on matrix on the te	sting set

Figure 10: Confusion matrix using GasHis-Transformer. The first column to the second column represents the confusion matrices for the classification results on the validation set, on the testing set.

is a critical evaluation metric to evaluate a model.

GasHis-transformer is used to train the H&E gastric histopathology image dataset for 75 epochs. AdamW optimizer [46] is used to optimization and its parameters set learning rate as 2e-3, eps as 1e-8, betas as [0.9,0.999], and weight decay as 1e-2. Furthermore, four criteria of the validation set and the testing set are calculated respectively to determine whether the model has convergence and generalization ability. The experimental results show that using GasHis-Transformer model to classify H&E gastric image dataset has incomparable performance. The confusion matrix using GasHis-Transformer on the validation set and testing set is shown in Fig. 10. On the validation set, 206 abnormal images and 209 normal images are classified into the appropriate categories. Only 4 abnormal images are misclassified into normal category and 1 normal image is misclassified into abnormal category. In GHIC tasks, because it is not meant to calculate the average precision and recall of binary classification problems, and combined with clinical application, the precision and recall of abnormal category and the accuracy and F1-score of all categories are selected in the evaluation metric. Overall, the accuracy, precision, recall, and F1-score of the classification in the validation set is 98.8%, 99.5%, 98.1%, and 98.8%, respectively. On the testing set, 403 abnormal images and 420 normal images are classified into the appropriate categories. Only 17 abnormal images are misclassified into normal category and even no normal images are misclassified into abnormal category. The accuracy, precision, recall, and F1-score of the classification is 98.0%, 100.0%, 96.0%, and 98.0%, respectively.

Four criteria have high scores on the validation set and testing set, and the difference of four criteria between validation set and testing set is narrow, which can explain that GasHis-Transformer has excellent generalization ability.

4.2.2. Contrast experiment

In order to show the excellent performance of GasHis-Transformer in GHIC task, a contrast experiment to to measure four metrics on the test set has been done which compared classification performance on the testing set with seven classical CNN models, including VGG-16, VGG-19 [22], Inception-V3 [12], ResNet-50 [11], Xception [27], ViT [33], and BoTNet-50 [31]. In addition, since VGG models do not converge at the learning rate of 2e-3 using AdamW optimizer, an extra comparative experiment with a low learning rate is conducted. Finally, to prove that the image normalization leads to an excellent consequence in the whole process, GasHis-Transformer and seven classical CNN models are compared using image normalization and without image normalization.

The experimental settings of these seven classical CNN models and something else such as optimization are briefly conducted as follows. To avoid the impact of all hyperparameters, all hyperparameters common to each model are set to the same value. First, all models use common size 224×224 pixels of input images. Second, AdamW solves the problem of parameter over-fitting with Adam optimizer by introducing L2 regularization terms of parameters in the loss function. It is the fastest optimizer for gradient descent speed and training neural networks which are used in all

Table 4
Four criteria of two-class on Grasic Dataset.([In %].)

Model	Precision	Recall	F1-score	Accuracy
GasHis-Transformer	100.0	96.0	98.0	98.0
Xception	100.0	94.3	97.1	97.1
BotNet-50	97.8	94.0	96.0	95.9
ResNet-50	96.8	95.0	96.0	95.9
Inception-V3	98.4	88.3	93.5	93.1
VGG-16	0.0	0.0	33.4	50.0
VGG-19	51.5	100.0	33.4	52.9
ViT	85.8	71.9	80.0	78.2

Table 5
Comparison of learning rate between 2e-3 and 2e-4 using VGG-16 and VGG-19.([In %].)

Model	Learning rate	Precision	Recall	F1-score	Accuracy
GasHis-Transformer	2e-3	100.0	96.0	98.0	98.0
VGG-16	2e-4	89.1	87.9	88.5	88.5
VGG-16	2e-3	0.0	0.0	33.4	50.0
VGG-19	2e-4	85.5	91.2	88.3	87.8
VGG-19	2e-3	51.5	100.0	33.4	52.9

models and its parameters setting is common with GasHis-Transformer, that is, learning rate as 2e-3, eps as 1e-8, betas as [0.9,0.999], and weight decay as 1e-2 [46, 47]. Finally, the whole training process of all models takes 75 epochs, and the learning rate adjustment strategy is used, that is, if the set loss function is not decreased within 15 epochs, the learning rate is reduced by ten times. The H&E gastric histopathological image dataset classification result of all models is shown in Table 4. What stands out in the table is easy to observe, that GasHis-Transformer using normalization achieves excellent performance in terms of precision, F1-score, and accuracy. Compared with the single BoTNet-50, the precision, recall, F1-score, and accuracy of GasHis-Transformer cascaded with GIM and LIM improves by 2.2%, 2.4%, 2.3%, 2.3%, and 2.3%, respectively; compared with the single Inception-V3, these four metrics improved by 1.6%, 8.1%, 5.1%, 4.7%, respectively. Furthermore, GasHis-Transformer has some improvement compared to Xception which is the best performing of the seven traditional CNN models. The two models are equal in precision, and the proposed GasHis-Transformer has a higher recall, F1-score, and accuracy than Xception by about 1.5% or so. Although the recall of GasHis-Transformer is not as higher as that of VGG-19, that has resulted from the nonconvergence of the network at a learning rate of 2e-3. F1score of VGG-19 only achieves 33.3%, indicating that it classifies all the data in the test set as abnormal, and consequently it can be concluded that the network does not converge. The same problem also arises for VGG-16. In summary, a comparison of different learning rates based on VGG models is conducted.

The comparison of learning rates between 2e-3 and 2e-4 in VGG models is shown in Table 5. What is striking about the figures in this table is VGG models converge at a learning

rate of 2e-4. What is striking about the figures in this table is VGG model converges at a learning rate of 2e-4. Although the recall rate decreases compared to the previous one, the model converges as a consequence of the substantial increase in F1-score. Thus, GasHis-Transformer has the highest recall as well as other metrics including precision, F1-score, and accuracy when compared to the converged VGG model with reduced learning rate and other previously converged CNN models.

Finally, the result of comparison of pre-processing whether using normalization is shown in Fig. 11. The comparison is performed at VGG-16 and VGG-19 using a learning rate of 2e-4 together with other networks using the original method. There is a clear trend of increasing these four criteria when using normalization. For the precision, the results obtained using normalization have a significant improvement except for ResNet-50 and Xception, and ViT even has a significant improvement of 23.4%. Other models including GasHis-Transformer, BoTNet-50, Inception-V3, VGG-16, and VGG-19 improve by 5.1%, 5%, 5.5%, 5.5%, and 6.5%, respectively. The criteria of Xception remain constant after using normalization, and only the criteria of ResNet-50 becomes worse after using normalization. For recall, while Inception-V3, VGG-16, VGG-19, and ViT have different degrees of reduction after using normalization, models with high classification outcomes including GasHis-Transformer, Xception, BoTNet-50, and ResNet-50 all have an improvement of about 3%. For F1-score and accuracy, which are the comprehensive criteria for evaluating a model's performance, all models show some improvement after using normalization, with GasHis-Transformer improving both F1-score and accuracy by 4.2%. In summary, the use of normalization in image preprocessing promotes four metrics of all models.

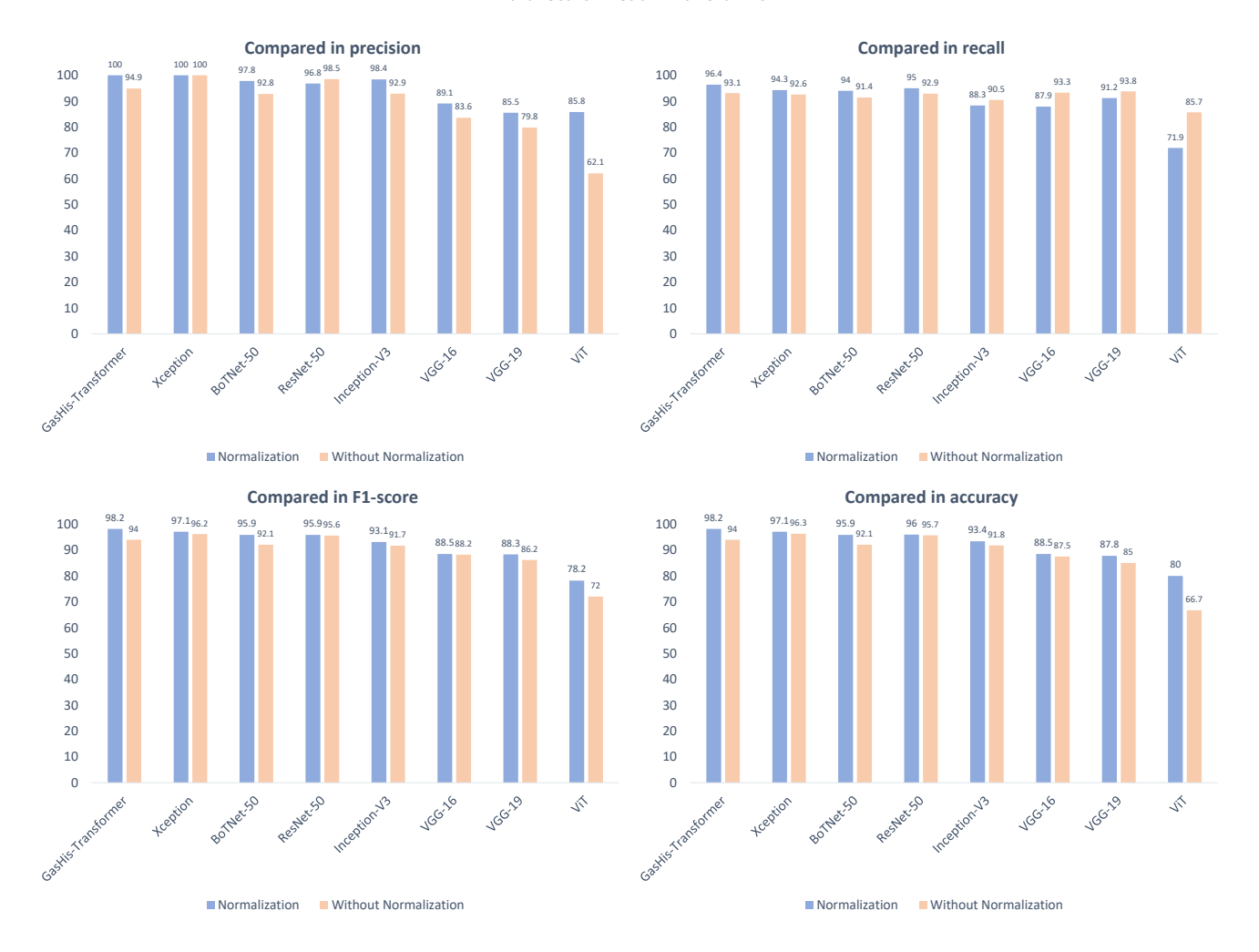


Figure 11: Comparison of pre-processing whether using normalization.

4.3. Extended experiment

The extended experiments are performed on the publicly available lymphoma dataset [48] and breast cancer dataset [49] following an experimental procedure for classification of the histopathological images of gastric cancer and performing several detail modifications which combining their characters of datasets to investigate further the favorable performance of the proposed GasHis-Transformer. Because three-classification and four-classification are used in extended experiments instead of two-classification, the average value of the overall category is taken as the evaluation criterion for all four criteria in extended experiments.

4.3.1. Extended experiment on lymphoma dataset

Malignant lymphoma is a cancer that affects the lymph nodes. Three types of malignant lymphomas are representative in the dataset: chronic lymphocytic leukemia (CLL), follicular lymphoma (FL) and mantle cell lymphoma (MCL) [50] as shown in Fig. 12. There are some examples in the lymphoma histopathological image dataset. The distribution of lymphoma cancer datasets for training, validation, and testing is shown in Table 6. A total of 374 images of different cancer categories are available in the lymphoma dataset. The

Table 6Distribution of lymphoma cancer datasets for training, validation and testing.

Image tpye	Training	Validation	Test	Sum
CLL	40	30	43	113
FL	40	30	69	139
MCL	40	30	52	122

Table 7
Data augmentation of lymphoma cancer datasets for training, validation and testing.

Image tpye	Training	Validation	Test	Sum
CLL	960	720	1032	2712
FL	960	720	1656	3336
MCL	960	720	1248	2928

number of CLL images is 113, the number of FL images is 139, and the number of MCL images is 122. All images in the lymphoma dataset are 1388×1040 pixels in size and ".tif" format. The data augmentation of lymphoma cancer

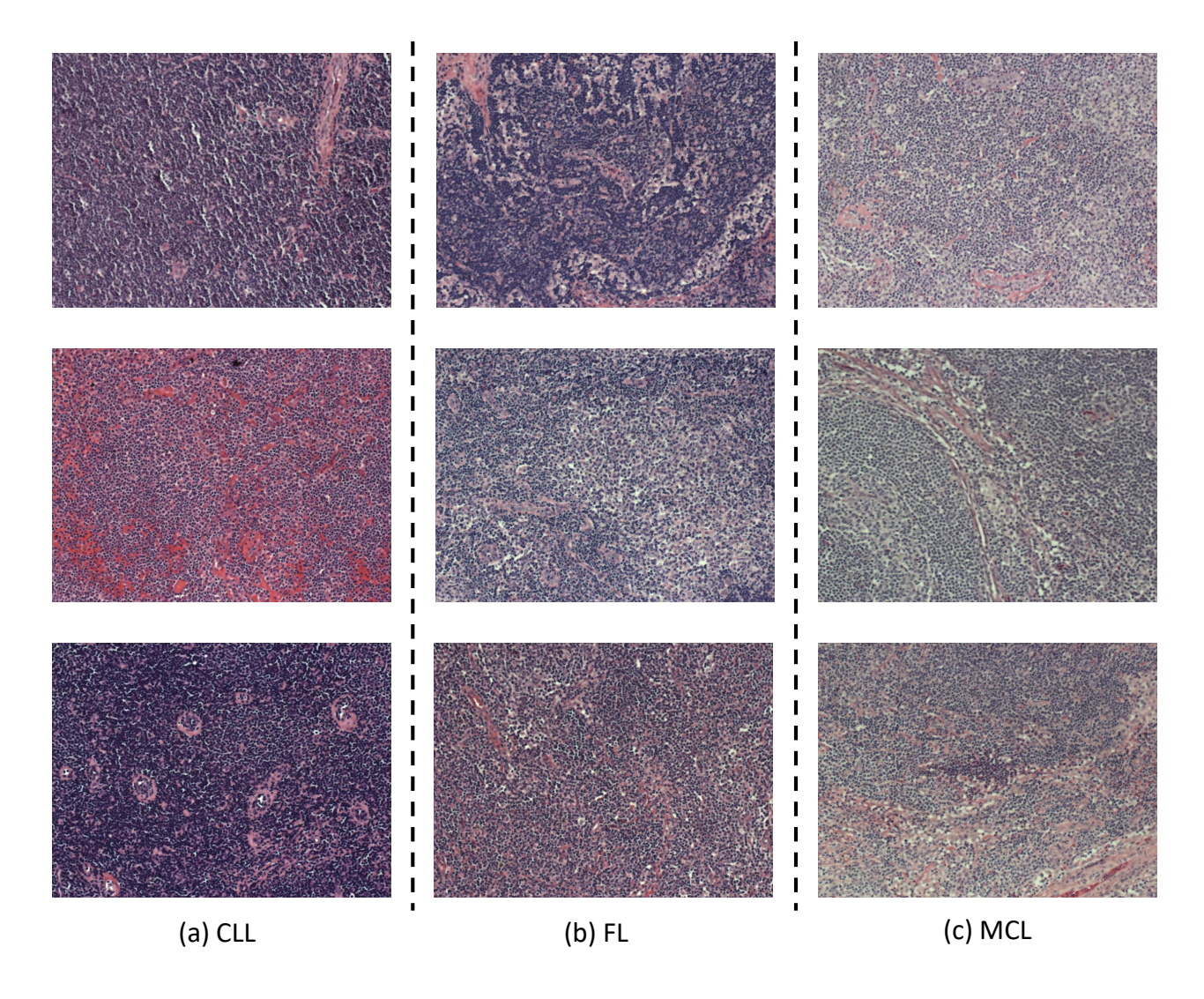


Figure 12: Some examples in the lymphoma image dataset.

datasets for training, validation, and testing is shown in Table 7. Since three different types of lymphoma are classified according to the shape of lymphocytes, directly resizing the image of lymphoma makes it difficult to distinguish the small and dense lymphocytes. Therefore, we crop the whole lymphoma image into 224×224 pixels as the standard input of GasHis-Transformer to expand the datasets by 24 times.

Table 8 below illustrates four metrics using GasHis-Transformer, Inception-V3 [12], ResNet-50 [11], Xception [27], ViT [33], and BoTNet-50 [31] at learning rate as 2e-3 and VGG-16 and VGG-19 [22] at the learning rate as 2e-4 to classify three-class lymphoma dataset which like something has been done in gastric dataset. GasHis-Transformer has the best performance in all four metrics compared with other traditional CNN models. In the lymphoma dataset, the best performance of the traditional CNN model is Inception-V3, Inception-V3 has the highest precision, recall, F1-score, and accuracy in traditional CNN models, which are 79.0%, 78.7%, 78.7%, and 80.2%, respectively. However, the performance

of GasHis-Transformer is even better than that of Inception-V3. The precision, recall, F1-score, and accuracy of GasHis-Transformer reached an outstanding 82.6%, 83.0%, 82.8%, 83.9%,respectively. Compared with Inception-V3, it has improved by 2.9%, 3.0%, 2.9%, 2.0%, respectively. Therefore, on lymphoma dataset, like on gastric cancer dataset, GasHis-Transformer exhibits favorable classification skills.

4.3.2. Extended experiment on breast cancer dataset

Breast cancer (BC) is considered the most common type of cancer amongst women. Breast cancer is associated with a high mortality rate in comparison to other cancers [51]. We further demonstrate the well-performance of GasHis-Transformer using the publicly available BreakHis dataset about breast cancer [49]. To date, the dataset consists of 7909 images at various magnifications including 40×, 100×, 200×, and 400×, categorized into benign and malignant tumors. The size of images is 700 × 460 pixels and with ".png" format. Both benign and malignant breast tumors can be

Table 8 Four criteria of three-class on Lymphoma Dataset. ([In %].)

Model	Precision	Recall	F1-score	Accuracy
GasHis-Transformer	82.6	83.0	82.8	83.9
Xception	79.7	79.4	78.4	80.1
BotNet-50	79.0	78.7	78.7	80.2
ResNet-50	78.7	79.3	78.6	79.7
Inception-V3	79.7	80.0	79.9	80.9
VGG-16	75.3	75.7	75.4	76.9
VGG-19	76.8	77.3	76.8	77.8
ViT	71.4	72.3	71.2	72.6

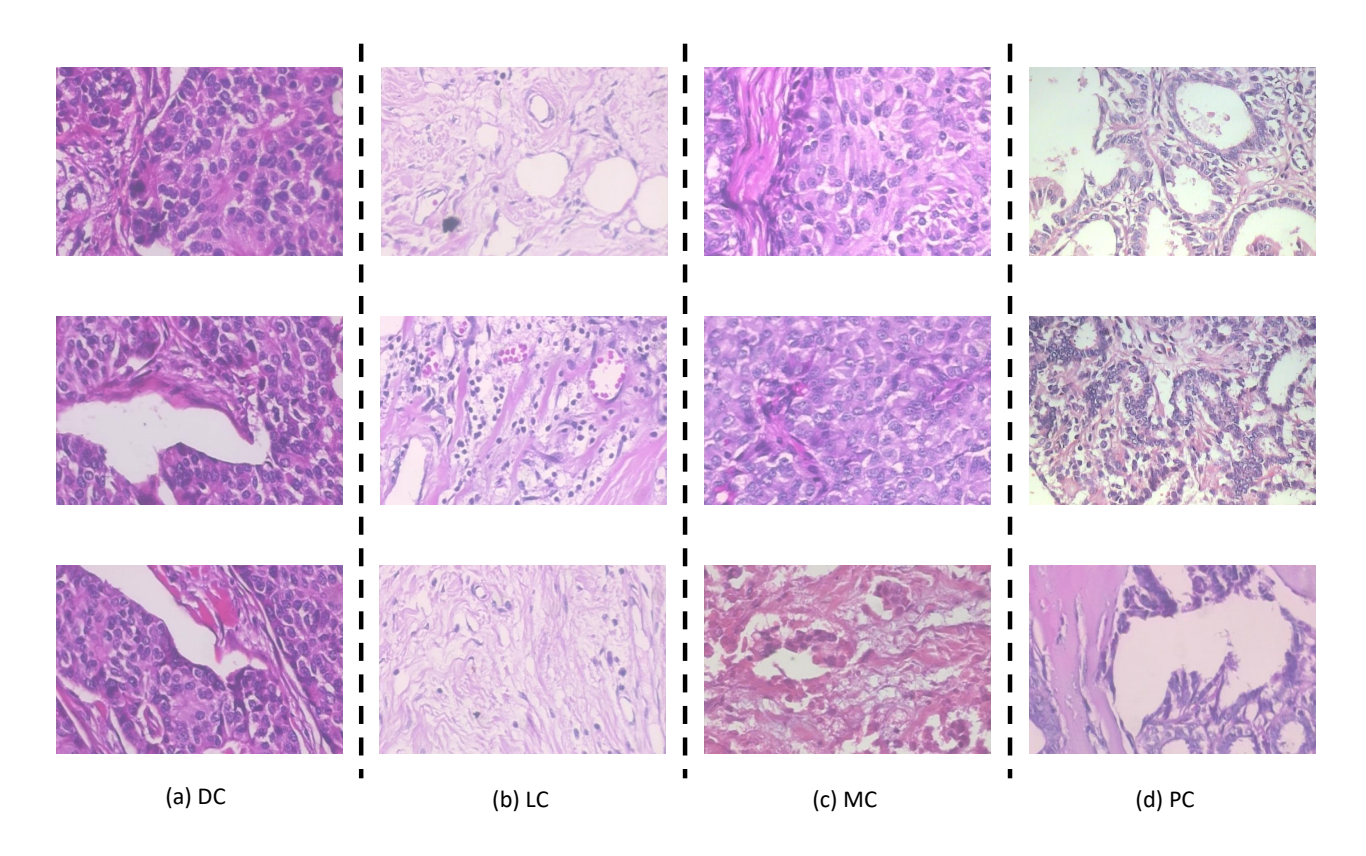


Figure 13: Some examples in the section of BreakHis dataset.

Table 9Distribution of BreakHis datasets for training, validation and testing.

Image tpye	Training	Validation	Test	Sum
DC	538	179	179	896
LC	98	33	32	163
MC	118	39	39	196
PC	81	27	27	135

classified into four different types each by the type of tumor. Only malignant tumors with a magnification of $200\times$ are used for the four classifications including ductal carcinoma (DC), lobular carcinoma (LC), mucinous carcinoma (MC), and papillary carcinoma (PC) of the breast. Some

 $\begin{tabular}{ll} \textbf{Table 10}\\ \textbf{Data augmentation of BreakHis datasets for training, validation and testing.} \end{tabular}$

Image tpye	Training	Validation	Test	Sum
DC	3228	1074	1074	5376
LC	588	198	192	978
MC	708	234	234	1176
PC	486	162	162	810

examples of these four different categories of breast cancer images are presented in Fig. 13 and the original data division is shown in Table 9. The original data is partitioned with a ratio of 6: 2: 2 for training, validation, and test sets. The data augmentation in the same way as the gastric cancer dataset

Table 11
Four criteria of four-class on BreakHis Dataset.([In %].)

Model	Precision	Recall	F1-score	Accuracy
Gathis-Transformer	85.3	86.1	85.6	89.4
Xception	80.1	80.3	80.2	86.0
BotNet-50	77.0	74.2	74.8	83.6
ResNet-50	71.7	74.7	72.7	81.3
Inception-V3	88.0	84.6	84.2	88.0
VGG-16	80.9	76.2	77.7	84.5
VGG-19	79.8	80.6	80.1	85.6
ViT	70.9	77.5	73.6	80.1

Table 12
The parameter size (MB) and training time (hour) of all eight models.

Model	Parameter size	Training time		
		Gastric	Lymphoma	Breast cancer
GasHis-Transformer	155	0.86	2.39	2.78
Xception	79	0.75	1.75	2.36
BoTNet-50	72	0.69	1.46	1.72
ResNet-50	90	0.69	1.46	1.73
Inception-V3	83	0.73	1.58	1.58
VGG-16	268	0.78	1.78	2.39
VGG-19	298	0.81	2.01	2.76
ViT	48	0.69	1.29	1.58

is shown in Table 10.

A same experimental parameter setting is used for the classification of the BreakHis dataset as for the gastric cancer dataset and the lymphoma dataset, likewise compare four metrics with VGG models with a learning rate of 2e-4 and other models with a learning rate of 2e-3 to demonstrate that GasHis-Transformer maintains a strong performance on the breast cancer dataset. The best classification result of traditional CNN models on breast cancer dataset is similar to the lymphoma dataset, which is obtained by Inception-V3, where four metrics including precision, recall, and F1score, and the accuracy rates are 88.0%, 84.6%, 84.2%, and 88.0%, respectively. Compared with Inception-V3, although the precision of GasHis-Transformer decreases marginally, its recall, F1-score, and accuracy are increased by 1.5%, 1.4%, and 1.4%, respectively. While a high precision can only demonstrate the conservativeness of the models and only forecast highly sure samples, F1-score is a comprehensive indicator for determining a model, so it shows that GasHis-Transformer has better image classification performance on the breast cancer dataset.

The expansion experiments on the lymphoma dataset and breast cancer dataset demonstrate that GasHis-Transformer is not only outstanding in GHIC tasks, but also capable in other histopathological image classification tasks of cancer. It further illustrates that GasHis-Transformer, which uses GIM and LIM, combined for the advantages of CNN and Transformer models that can extract local or global features, and its classification metrics exceed those of the current predominant CNN and Transformer models.

4.4. Computational time and experimental environment

Finally, the computation time of GasHis-Transformer model is briefly depicted. Table 12 shows the parameter size and training time on three different datasets of all eight models including GasHis-Transformer, Xception, BoTNet-50, ResNet-50, Inception-V3, VGG-16, VGG-19, and ViT. A workstation with Windows 10, AMD Ryzen 7 4800HS with Radeon Graphics with 2.90 GHz, GeForce RTX 2060 with 6 GB and 16 GB RAM is utilized in the experiment. The Matlab of R2020b is utilized to do the pre-processing of original image. When training GasHis-Transformer, Xception, BoTNet-50, ResNet-50, Inception-V3, VGG-16, VGG-19, and ViT networks, PyTorch v1.6 framework of Python 3.6 is deployed.

4.5. Misclassification analysis

There are significant discrepancies among the misclassification problems that remain to be overcome, and in order to analyze the causes of misclassification, some example is shown in Fig. 14. In conjunction with medical knowledge from our collaborating histopathologists, the reasons for image misclassification are as follows.

First, because of the complex components of histopathological images of gastric cancer, in which the features between normal and abnormal regions are inconspicuous, it leads to difficulties in image feature extraction. Second, some abnormal images have the majority of regions as normal regions and just a few as abnormal regions, and the attention mechanism primarily used in the proposed GasHis-Transformer

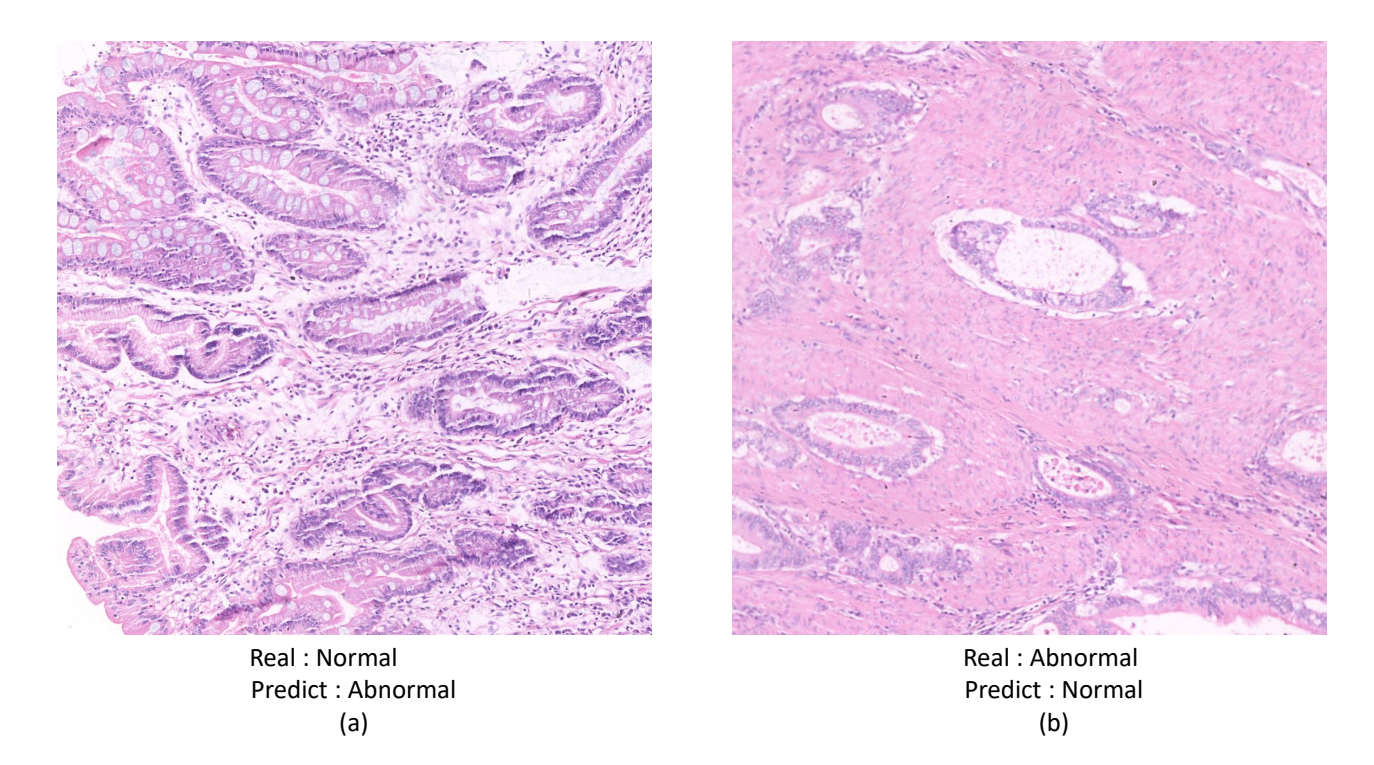


Figure 14: Typical examples of the misclassification results.

is not effective in describing all spatial in this case.

5. Conclusion and future work

In this paper, we propose a GasHis-Transformer to classify histopathological images of gastric cancer as normal or abnormal in a binary classification of benign and malignant. This approach not only considers the advantages of classical CNN model in extracting local features but also uses the most recent Transformer model. This model combines the global and local associations of images in a spatial context. In the experiment, the method is tested on a gastric cancer histopathology dataset with an accuracy of 98.0% for classification in general, which demonstrates the potential in GHIC tasks. Besides, we conducted extended tests on the lymphoma dataset and the breast cancer dataset with accuracies of 83.9%, and 89.4%, respectively, demonstrating the generalization capability of GasHis-Transformer on histopathology images.

In our future work, we are planning to increase the volume of data in a single dataset, allowing the same doctors to expand the data. This will allow testing the model not only on gastric cancer but also on more cancer types, such as liver or intestinal cancer. In addition, we only use the Transformer model without any modifications, and in the future, we will try to improve the Transformer model by adding or reducing the network layer structure.

References

- O. M. Yis, G. Bugdayci, M. B. Pehlivan, M. Basol, Roles of the systemic inflammatory response biomarkers in the diagnosis of cancer patients with solid tumors, Experimental Biomedical Research 2 (2019) 37–43.
- [2] A. O.-O. Chan, B. C.-Y. Wong, S.-K. Lam, Gastric cancer: past, present and future, Canadian Journal of Gastroenterology 15 (2001) 469–474
- [3] H. Sharma, N. Zerbe, D. Heim, S. Wienert, H.-M. Behrens, O. Hell-wich, P. Hufnagl, A multi-resolution approach for combining visual information using nuclei segmentation and classification in histopathological images., in: VISAPP (3), 2015, pp. 37–46.
- [4] S. A. Korkmaz, H. Bínol, A. Akçiçek, M. F. Korkmaz, A expert system for stomach cancer images with artificial neural network by using hog features and linear discriminant analysis: Hog_lda_ann, in: 2017 IEEE 15th International Symposium on Intelligent Systems and Informatics (SISY), IEEE, 2017, pp. 000327–000332.
- [5] T. M. Elsheikh, R. M. Austin, D. F. Chhieng, F. S. Miller, A. T. Moriarty, A. A. Renshaw, American society of cytopathology workload recommendations for automated paptest screening: Developed by the productivity and quality assurance in the era of automated screening task force, Diagnostic cytopathology 41 (2013) 174–178.
- [6] K. Doi, Computer-aided diagnosis in medical imaging: historical review, current status and future potential, Computerized medical imaging and graphics 31 (2007) 198–211.
- [7] K. Doi, Current status and future potential of computer-aided diagnosis in medical imaging, The British journal of radiology 78 (2005) 83–819.
- [8] N. Asiri, M. Hussain, F. Al Adel, N. Alzaidi, Deep learning based computer-aided diagnosis systems for diabetic retinopathy: A survey, Artificial intelligence in medicine 99 (2019) 101701.
- [9] Y. LeCun, Y. Bengio, G. Hinton, Deep learning, nature 521 (2015) 436–444
- [10] Y. LeCun, B. Boser, J. S. Denker, D. Henderson, R. E. Howard, W. Hubbard, L. D. Jackel, Backpropagation applied to handwritten

- zip code recognition, Neural computation 1 (1989) 541–551.
- [11] K. He, X. Zhang, S. Ren, J. Sun, Deep residual learning for image recognition, in: Proceedings of the IEEE conference on computer vision and pattern recognition, 2016, pp. 770–778.
- [12] C. Szegedy, V. Vanhoucke, S. Ioffe, J. Shlens, Z. Wojna, Rethinking the inception architecture for computer vision, in: Proceedings of the IEEE conference on computer vision and pattern recognition, 2016, pp. 2818–2826.
- [13] N. I. Yassin, S. Omran, E. M. El Houby, H. Allam, Machine learning techniques for breast cancer computer aided diagnosis using different image modalities: A systematic review, Computer methods and programs in biomedicine 156 (2018) 25–45.
- [14] H. Sharma, N. Zerbe, C. Böger, S. Wienert, O. Hellwich, P. Hufnagl, A comparative study of cell nuclei attributed relational graphs for knowledge description and categorization in histopathological gastric cancer whole slide images, in: 2017 IEEE 30th International Symposium on Computer-Based Medical Systems (CBMS), IEEE, 2017, pp. 61–66.
- [15] S. A. Korkmaz, H. Binol, Classification of molecular structure images by using ann, rf, lbp, hog, and size reduction methods for early stomach cancer detection, Journal of Molecular Structure 1156 (2018) 255–263.
- [16] B. Liu, M. Zhang, T. Guo, Y. Cheng, Classification of gastric slices based on deep learning and sparse representation, in: 2018 Chinese Control And Decision Conference (CCDC), IEEE, 2018, pp. 1825– 1820
- [17] E. Garcia, R. Hermoza, C. B. Castanon, L. Cano, M. Castillo, C. Castanneda, Automatic lymphocyte detection on gastric cancer ihe images using deep learning, in: 2017 IEEE 30th international symposium on computer-based medical systems (CBMS), IEEE, 2017, pp. 200–204.
- [18] Z. Song, S. Zou, W. Zhou, Y. Huang, L. Shao, J. Yuan, X. Gou, W. Jin, Z. Wang, X. Chen, et al., Clinically applicable histopathological diagnosis system for gastric cancer detection using deep learning, Nature communications 11 (2020) 1–9.
- [19] S. C. Kosaraju, J. Hao, H. M. Koh, M. Kang, Deep-hipo: Multi-scale receptive field deep learning for histopathological image analysis, Methods 179 (2020) 3–13.
- [20] K.-O. Cho, S. H. Lee, H.-J. Jang, Feasibility of fully automated classification of whole slide images based on deep learning, The Korean journal of physiology & pharmacology: official journal of the Korean Physiological Society and the Korean Society of Pharmacology 24 (2020) 89.
- [21] A. Krizhevsky, I. Sutskever, G. E. Hinton, Imagenet classification with deep convolutional neural networks, Advances in neural information processing systems 25 (2012) 1097–1105.
- [22] K. Simonyan, A. Zisserman, Very deep convolutional networks for large-scale image recognition, arXiv preprint arXiv:1409.1556 (2014).
- [23] W. Rawat, Z. Wang, Deep convolutional neural networks for image classification: A comprehensive review, Neural computation 29 (2017) 2352–2449.
- [24] C. Szegedy, W. Liu, Y. Jia, P. Sermanet, S. Reed, D. Anguelov, D. Erhan, V. Vanhoucke, A. Rabinovich, Going deeper with convolutions, in: Proceedings of the IEEE conference on computer vision and pattern recognition, 2015, pp. 1–9.
- [25] Z. Lu, Y. Bai, Y. Chen, C. Su, S. Lu, T. Zhan, X. Hong, S. Wang, The classification of gliomas based on a pyramid dilated convolution resnet model, Pattern Recognition Letters 133 (2020) 173–179.
- [26] L. Sifre, S. Mallat, Rigid-motion scattering for texture classification, arXiv preprint arXiv:1403.1687 (2014).
- [27] F. Chollet, Xception: Deep learning with depthwise separable convolutions, in: Proceedings of the IEEE conference on computer vision and pattern recognition, 2017, pp. 1251–1258.
- [28] A. G. Howard, M. Zhu, B. Chen, D. Kalenichenko, W. Wang, T. Weyand, M. Andreetto, H. Adam, Mobilenets: Efficient convolutional neural networks for mobile vision applications, arXiv preprint arXiv:1704.04861 (2017).

- [29] A. Vaswani, N. Shazeer, N. Parmar, J. Uszkoreit, L. Jones, A. N. Gomez, L. Kaiser, I. Polosukhin, Attention is all you need, arXiv preprint arXiv:1706.03762 (2017).
- [30] K. Han, Y. Wang, H. Chen, X. Chen, J. Guo, Z. Liu, Y. Tang, A. Xiao, C. Xu, Y. Xu, et al., A survey on visual transformer, arXiv preprint arXiv:2012.12556 (2020).
- [31] A. Srinivas, T.-Y. Lin, N. Parmar, J. Shlens, P. Abbeel, A. Vaswani, Bottleneck transformers for visual recognition, arXiv preprint arXiv:2101.11605 (2021).
- [32] S. Khan, M. Naseer, M. Hayat, S. W. Zamir, F. S. Khan, M. Shah, Transformers in vision: A survey, arXiv preprint arXiv:2101.01169 (2021).
- [33] A. Dosovitskiy, L. Beyer, A. Kolesnikov, D. Weissenborn, X. Zhai, T. Unterthiner, M. Dehghani, M. Minderer, G. Heigold, S. Gelly, et al., An image is worth 16x16 words: Transformers for image recognition at scale, arXiv preprint arXiv:2010.11929 (2020).
- [34] I. Bello, B. Zoph, A. Vaswani, J. Shlens, Q. V. Le, Attention augmented convolutional networks, in: Proceedings of the IEEE/CVF International Conference on Computer Vision, 2019, pp. 3286–3295.
- [35] P. Shaw, J. Uszkoreit, A. Vaswani, Self-attention with relative position representations, arXiv preprint arXiv:1803.02155 (2018).
- [36] P. Ramachandran, N. Parmar, A. Vaswani, I. Bello, A. Levskaya, J. Shlens, Stand-alone self-attention in vision models, arXiv preprint arXiv:1906.05909 (2019).
- [37] G. D. Finlayson, B. Schiele, J. L. Crowley, Comprehensive colour image normalization, in: European conference on computer vision, Springer, 1998, pp. 475–490.
- [38] J. Huang, L. Qu, R. Jia, B. Zhao, O2u-net: A simple noisy label detection approach for deep neural networks, in: Proceedings of the IEEE/CVF International Conference on Computer Vision, 2019, pp. 3326–3334.
- [39] N. Srivastava, G. Hinton, A. Krizhevsky, I. Sutskever, R. Salakhutdinov, Dropout: a simple way to prevent neural networks from overfitting, The journal of machine learning research 15 (2014) 1929–1958.
- [40] P. Baldi, P. J. Sadowski, Understanding dropout, Advances in neural information processing systems 26 (2013) 2814–2822.
- [41] W. Liu, Y. Wen, Z. Yu, M. Yang, Large-margin softmax loss for convolutional neural networks., in: ICML, volume 2, 2016, p. 7.
- [42] C. Sun, C. Li, Y. Li, Data for hcrf, http://dx.doi.org/10.17632/ thgf23xgy7.2/, 2020. Mendeley data, v2.
- [43] M. Miettinen, J. Lasota, et al., Gastrointestinal stromal tumors (gists): definition, occurrence, pathology, differential diagnosis and molecular genetics, Pol J pathol 54 (2003) 3–24.
- [44] Y. Li, X. Li, X. Xie, L. Shen, Deep learning based gastric cancer identification, in: 2018 IEEE 15th International Symposium on Biomedical Imaging (ISBI 2018), IEEE, 2018, pp. 182–185.
- [45] P. Smith, Bilinear interpolation of digital images, Ultramicroscopy 6 (1981) 201–204.
- [46] I. Loshchilov, F. Hutter, Fixing weight decay regularization in adam (2018).
- [47] C. Cortes, M. Mohri, A. Rostamizadeh, L2 regularization for learning kernels, arXiv preprint arXiv:1205.2653 (2012).
- [48] E. Jaffe, N. Orlov, Nia intramural research program laboratory of genetics, https://ome.grc.nia.nih.gov/iicbu2008/lymphoma/index.html, 2008.
- [49] F. A. Spanhol, L. S. Oliveira, C. Petitjean, L. Heutte, A dataset for breast cancer histopathological image classification, Ieee transactions on biomedical engineering 63 (2015) 1455–1462.
- [50] K. Lennert, N. Mohri, H. Stein, E. Kaiserling, The histopathology of malignant lymphoma, British Journal of Haematology 31 (1975) 193–203.
- [51] A. G. Waks, E. P. Winer, Breast cancer treatment: a review, Jama 321 (2019) 288–300.